In Situ Thermal Interactions of Cu-Based Anti-Corrosion Coatings on Steel Implemented by Surface Alloying

Huda Hanif Khan [1,†] , Tong Wang [1,†] , Lihong Su [1], Huijun Li [1], Qiang Zhu [1], Ana Yang [2], Zigang Li [2], Wei Wang [2,*] and Hongtao Zhu [1,*]

1 School of Mechanical Materials Mechatronics and Biomedical Engineering, University of Wollongong, Wollongong, NSW 2522, Australia; hhk991@uowmail.edu.au (H.H.K.); tw874@uowmail.edu.au (T.W.); lihongsu@uow.edu.au (L.S.); huijun@uow.edu.au (H.L.); qzhu@uow.edu.au (Q.Z.)
2 Baosteel Central Research Institute, Baowu Steel Group Corporation, Shanghai 201900, China; yangan@baosteel.com (A.Y.); zigangli@baosteel.com (Z.L.)
* Correspondence: weiwang@baosteel.com (W.W.); hongtao@uow.edu.au (H.Z.)
† These authors contributed equally to this work.

Abstract: Incorporating expensive alloying elements into bulk steel for corrosion protection is undesirable, considering that only the surfaces are exposed to aggressive environments. Therefore, this work focused on developing and optimizing a new surface functioning technology through in situ observation of thermal interactions between the metallic powders at elevated temperatures. The study revealed that the Cu-Ni powder mixture, with 12.5 wt% Ni, began to melt at 1099.5 °C and was fully melted at 1175 °C, significantly different from the Cu-Ni solid solution and bulk Cu or Ni. As a result of high-temperature reactions, copper penetration of up to 35 μm for pure copper and 55 μm for copper-chromium composite coatings occurred due to liquid metal corrosion. In contrast, the copper-nickel composite coating exhibited a cupronickel solution microstructure with FeNi dendrites and a nickel-rich transition layer. This cupronickel coating, with a chemical composition of 89.3 wt% Cu, 6.2 wt% Ni, and 4.5 wt% Fe, demonstrated uniform thickness, superior surface morphology, and continuous coverage on the steel substrate. Furthermore, the Ni-rich transition layer played a vital role in preventing copper penetration along the grain boundary of the steel matrix while forming a chemical binding between the coating and the substrate. The practicality of the coating was further confirmed through the hot-rolling procedure and subsequent electrochemical corrosion tests, which resulted in a 44% improvement in corrosion resistance.

Keywords: surface alloying; anti-corrosion coating; cupronickel

1. Introduction

Corrosion poses a significant threat to the structural integrity of marine and offshore assets, which results in surface degradation, mechanical failure, environmental pollution, and loss of life. Steel, being a primary material used in various industries such as transportation, oil and gas, petrochemical, construction, and marine engineering, has been subject to numerous corrosion prevention methods throughout history [1], such as corrosion inhibitors, alloying, sacrificial anode, and protective coatings. Protective coatings, in particular, have proven to be effective in extending the service life of steel structures [2,3]. Examples of protective coatings include paints, organic/inorganic coatings, diffusion coatings, thermal spray metallic coatings, and galvanization [4–7]. Alloying, another essential methodology, involves adding alloying elements such as Cu, Cr, Ni, P, Si, and Mn to bulk steel. These elements help form a protective passivation layer, known as patina, on the surface when exposed to a corrosive environment, thus protecting the material underneath [8]. Both protective coatings and alloying have their advantages and limitations. Applying protective coatings is time-consuming and expensive, requiring complex procedures for surface preparation and application [9,10]. Alloying, on the other hand, involves adding expensive

elements to the bulk material when only the surface is exposed to harsh environments. Moreover, alloying could alter the material's mechanical properties of the bulk material, which is not always desirable.

Cu, Cr, and Ni are widely used alloying elements to enhance the corrosion resistance of steels. These elements facilitate the formation of an adhesive oxide layer when exposed to aggressive environments, thereby improving the product's service life [11]. Due to its low cost, copper is commonly introduced as a base alloying element. However, adding Cu can lead to hot shortness, a complex high-temperature chemical reaction process. The relatively low melting Cu-enriched phase liquefies at high temperatures and penetrates along the austenite grain boundaries of the steel matrix, resulting in cracking during processes like hot-rolling [12]. Ni plays a crucial role in preventing hot shortness by being noble compared to Fe, exhibiting less tendency to oxidize when oxide scales form on the steel surface. Furthermore, Ni and Cu are completely soluble in each other, increasing the melting point of the Cu-enriched liquid phase and restricting it from penetrating grain boundaries. Akamatsu et al. [13] found that the liquid phase decreases as the percentage of Ni increases, and no more liquid phase is observed when the percentage of Ni is equal to or greater than that of Cu. Yamamoto et al. [14] developed a new surface melting technology whereby the surface layer of the slab at the back of the continuous caster is uniformly melted utilizing plasma or electromagnetic heating. Ni, as a wire, is added as an alloying agent to the melted surface layer to prevent Cu in the surface layer from promoting hot shortness at subsequent rolling. The surface melting technology proves that Ni and Cu can be introduced on steel surfaces for anti-corrosion without incurring adverse hot shortness. Cupronickels, alloys of Cu and Ni, are known for their high resistance to corrosion and biofouling properties [15], which are widely used in marine engineering, coinage, and cryogenic applications [16]. Tolulope Loto [17] found that Cu-Ni 90/10 exhibited superior corrosion resistance at a high NaCl concentration solution, i.e., the corrosion rate of Cu-Ni 90/10 was just 0.74 mm/yr compared to the 2.68 mm/yr value of Cu–Zn 70/30 alloy at 4.5% NaCl concentration. The addition of Cr in steel is beneficial [18]. S. A. Park et al. [19] conducted electrochemical corrosion tests on low-alloy steel containing 0.1%, 0.3%, and 0.5% Cr after immersion in a chloride-containing environment for seven days and demonstrated that the addition of up to 0.3% Cr positively affected corrosion behavior, whereas 0.5% Cr promoted localized corrosion.

Surface alloying is an exciting technique to alter steel's surface properties without compromising the properties of the bulk material. It has been implemented for several different purposes, such as enhancing surface hardness, scratch resistance, corrosion resistance, etc. Carburizing, nitriding, boriding, chromizing, and aluminizing are examples of conventional surface alloying methods. Typically, this process involves heating the material at high temperatures and introducing the desired alloying element into the atmosphere in a gaseous or plasma state or through a sand bath. However, the material needs to be heated for several hours in the atmosphere to achieve the desired diffusion thickness [20]. It is crucial to select the appropriate temperatures and understand the thermal interactions between the alloying element particles and the steel surface at those temperatures when designing a surface alloying technique [21–23]. For example, the fully melted Cu-based coating could increase the risk of liquid metal embrittlement, leading to crack formation or complete failure during service [24–26]. In contrast, insufficient heating would not result in a solid solution for successful surface alloying [23].

Thermal analysis software such as Thermo-Calc can predict alloys' phase transformations and thermal behaviors based on their compositions under equilibrium conditions. However, these calculations rely on equilibrium conditions and are based on pre-alloyed materials that may or may not be achieved during the rapid heating and cooling of metallic powders. A high-temperature confocal laser scanning microscope has been extensively used by various researchers to observe in situ the thermal behaviors of alloys during heating or cooling processes [27–30]. It can capture real-time images of the specimen as it undergoes solidification or transforms into a liquid phase. It has been successfully employed

to study phase transformations, slag formation, dissolution of elements/compounds, and other helpful information [31,32]. Raman spectroscopy has also been widely used for in situ and operando exploration of material properties, real-time monitoring of high-temperature reactions, and understanding of high-temperature heat treatments. Böhme et al. [33] used a heating stage coupled with a Raman microscope to investigate the formation and stability properties of hydroxylapatite in situ. Molten salt chemistry has been explored using ultraviolet-visible (UV-vis) absorbance and Raman spectroscopy [34]. More recently, Zhang et al. [35,36] developed a customized in situ high-temperature fiber-optic Raman probe to reveal the structure of glass and slag and investigate in situ molten flux for continuous casting in steel manufacturing at temperatures up to 1400 °C.

Current research focuses on developing and optimizing a new surface alloying technology that can be implemented on commonly hot-rolled carbon steels by integrating Cu-based metallic compounds and steel matrix to form a corrosion-resistant surface coating. Unlike adding alloying elements to the bulk material, this technique solely alloys the surface, creating a protective coating without altering the properties of the bulk material. Surface alloying of steel at a high temperature presents a promising solution to improve the corrosion resistance of carbon steel at a low manufacturing cost.

The proposed approach combines and modifies surface diffusive coatings and thermal spray coating techniques to create a more cost-effective method that can be integrated into steel strip and plate manufacturing, eliminating the need for additional processing costs [37]. In conventional diffusion coating, the substrate surface gets enriched by the diffusing elements. However, no physical coating is developed, and the surface becomes an alloy of the substrate and the diffusing elements [38,39]. On the other hand, thermal spray coatings involve spraying hot coating materials onto the cold substrate surface, creating a layer on top, but adhesiveness is not as good as what could be achieved with the diffusion technique. Furthermore, the significant temperature difference between hot sprayed material and cold substrate can lead to the formation of cracks within the coating and coating-substrate interface, compromising the corrosion resistance of the coating [40–42]. Therefore, it is vital to combine and modify these methods by heating the alloying powders on the steel substrate to form a protective coating with a diffused interface. Moreover, the traditional surface alloying techniques are primarily designed for single-element coatings, whereas the proposed method can accommodate a combination of a few elements within a single coating process. For example, a cupronickel compound coating containing two metallic elements, Cu and Ni, is developed. Theoretical results from Thermo-Calc software 2024a with Database 'TCFE9' were used to design the experimental procedure and heating profiles. Based on these heating profiles, tests were conducted, and in situ observations were recorded using high-temperature confocal scanning laser microscopy.

2. Materials and Methodology

2.1. Materials

Coating materials were chosen by considering the effect of alloying elements on the corrosion properties of the steel, with particular attention to the synergistic impact of multi-elements [43]. Current work developed a new surface mitigation technology that integrates Cu, Ni, and Cr metallic powders with a steel matrix to form a robustly bonded, corrosion-resistant layer onto steel substrates. Cu is a base anti-corrosion element due to its cost-effective and appreciated melting point of 1083 °C, closely aligning with the working temperature in the hot rolling of carbon steel plates or strips [44,45]. The addition of Ni not only enhances the solubility/diffusion of Cu in the γ phase but also increases the melting point of the Cu-rich compound, which prevents the adverse impact of hot shortness [46]. The inclusion of Cr helps improve the corrosion resistance; however, the high affinity of Cr could make it sensitive to high-temperature oxidation. It is essential to report that both Cr and Ni have higher melting points, 1907 °C and 1455 °C, respectively, which can help to maintain a solid-liquid state at working temperature instead of a fully molten liquid. Since

the alloying elements are only applied to the surface of the steel instead of the bulk of the steel, this approach offers significant cost savings.

Q235 steel (99.13% Fe, 0.1637% C, 0.67 Mn, 0.022 Si, and traces of sulfur) was introduced as the steel substrate for the current investigation. Q235 steel and its ASTM equivalent A36 are prevalent in structural applications, such as bridges and boiler support structures, etc., due to its superior plasticity, toughness, weldability, cold bending performance, and adequate strength, along with low price compared to other steel grades and alloyed steels.

In this research, we utilized Cu powder (particle size of 45 μm, purity of 99%, and density of 3–3.8 g/cm^3), Cr powder (particle size of 5 μm, purity of 99%), and Ni powder (particle size of 1 μm, purity of 99%). Three distinct coating powder combinations, including (1) pure Cu, (2) a mixture of 87.5 wt% Cu and 12.5 wt% Ni, and (3) a mixture of 90 wt% Cu and 10 wt% Cr, were developed to explore the proposed surface alloying techniques. Each component was individually weighed using a physical scale and then mixed thoroughly together.

The ratio of Cu and Ni mixture was selected based on cupronickel 90/10 alloy, known for its exceptional corrosion-resistive properties. Furthermore, a marginally increased proportion of Ni to 12.5 wt% was chosen due to Ni's solubility in Fe at high temperatures, potentially forming a barrier that prevents Cu from penetrating deeper into the substrate's grain boundaries. The Cu–Cr weight ratio was maintained at 9:1, a slight reduction of Cr compared to Ni in the Cu-Ni mixture, taking into account the higher melting point of Cr and its insolubility in Cu.

2.2. Experimental Setup for In Situ Observation and Designing Thermal Profiles

The in situ and real-time thermal interactions of the designed metallic coatings were investigated with a high-temperature confocal laser scanning microscope (HTCLSM), which simulates the operational conditions of an industrial reheating furnace in a hot strip mill. The HTCLSM, manufactured by Lasertec Corporation, Yokohama, Japan, features a vacuum chamber-type heating furnace that allows observation under various conditions, such as in a vacuum, with inert gas, or in a reducing atmosphere. The confocal optics enable the observation and video recording of the melting and solidification process without interference from the high-intensity light emitted at elevated temperatures. The observation and recording of the melting and solidification process of Cu-coated samples were correlated with the actual temperature and thermal history/profiles employed during heating and cooling. This correlation helps in understanding phase transitions and microstructural evolution influenced by specific heating and cooling profiles and rates.

Round, thin Q235 specimens of 5.5 mm in diameter and 2.2 mm in thickness were sectioned from the steel plate and then polished using a Struers Tegramin grinding and polishing machine (Copenhagen, Denmark) for in situ high-temperature observation.

Cu-Ni alloy is recognized as an isomorphous system known for its ability to form solid solutions over a range of temperatures [47]. As shown in Figure 1, we used Thermo-Calc software to calculate the Cu-Ni binary phase diagram. The results indicate that the solidus and liquidus temperatures for the designed Cu-Ni coating with a 12.5 wt% Ni are 1137.5 °C and 1162.5 °C, respectively. In Figure 1, α_1 represents a Cu solid solution with an fcc structure and α_2 denotes a Ni fcc-solid solution, which shows a miscibility gap in the Cu-Ni phase diagram at lower temperatures. Hence, a temperature above the liquidus temperature, 1250 °C, was selected to investigate the melting and solidification process through HTCLSM. This temperature is commonly employed in actual heating and reheating furnaces for hot steel manufacturing. The same heating temperature was chosen for the Cu–Cr coating as well. However, for the pure Cu powder coating, a slightly low temperature of 1200 °C was selected, considering the low melting point of Cu. In contrast, the Cu–Cr binary system exhibits very limited solubility between the two elements, with nearly no solubility up to 1076 °C.
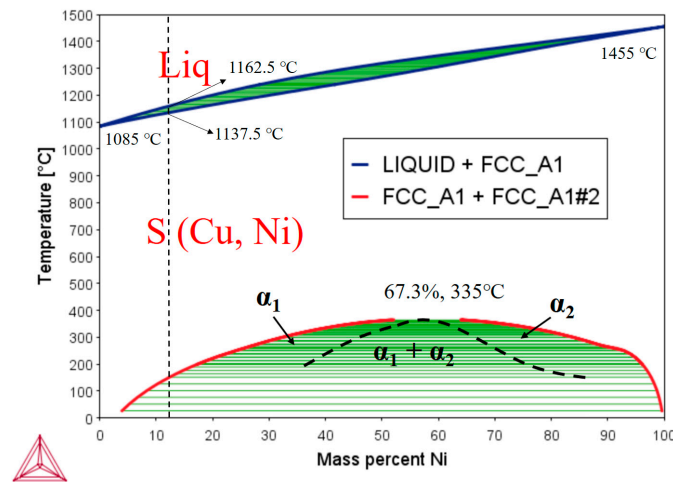
Figure 1. Cu-Ni binary phase diagram calculated by Thermo-Calc software.

Figure 2 presents our designed thermal profiles of three coatings used in HTCLSM experiments. In the pure Cu experiment, as shown in Figure 2a, the Q235 substrate and coating powder were heated to 800 °C at a rate of 100 °C/min, which is below Cu's melting point of 1085 °C. Following this, the temperature was increased to 1200 °C at a reduced rate of 50 °C/min. Then, the temperature was maintained at 1200 °C for 10 min before cooling down to 800 °C at a rate of 10 °C/min and followed by rapid cooling to 200 °C at a rate of 100 °C/min. For the samples covered with Cu-Ni and Cu–Cr powder composites, as depicted in Figure 2b, the samples were heated to 1250 °C at a rate of 100 °C/min and then held at this temperature for 10 min. After that, the samples were cooled to 1050 °C with a 20 °C/min cooling rate and then further reduced to 200 °C at a cooling rate of 100 °C/min. The HTCLSM furnace chamber was filled with argon gas at a flow rate of 0.4 LPM to protect the samples from severe oxidation during the testing process.
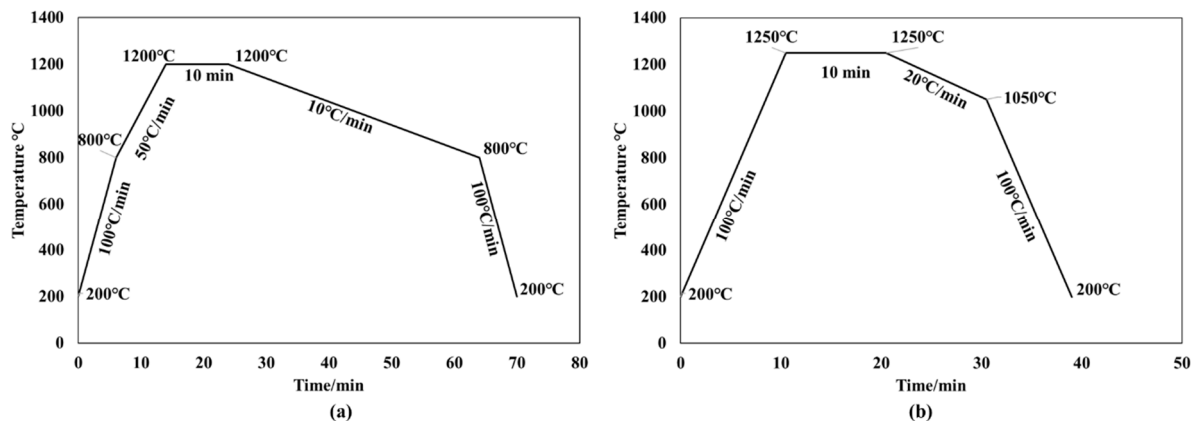

Figure 2. Thermal setup of (**a**) pure Cu, (**b**) Cu-Ni, and Cu–Cr coatings for HTCLSM experiments.

2.3. Coating Performance Characterization

Following the in situ observation, the top surface and cross-section of the samples along the radial plane were exanimated using optical microscopy (OM), scanning electron microscopy (SEM), and energy dispersive spectrometry (EDS) in terms of surface morphology, coating thickness, microstructure, and the bonding and diffusion behaviors between the coating layer and Q235 substrate.

3. Results and Discussion

3.1. In Situ Phase Transformation of Coatings

The melting and solidification behavior of Cu, Cu-Ni, and Cu–Cr composite coatings on Q235 steel substrates were influenced by the microstructure, phase composition, thermal properties, and interfacial interactions between the composites and the steel substrate.

Figure 3 displays the melting and solidification process of the pure Cu-coated samples, subject to the thermal history detailed in Figure 2a. It can be found that Cu powder was uniformly dispersed on the top surface of the Q235 substrate, as evidenced by an in situ image at 641 °C prior to melting. The in situ observation revealed that the Cu powder started melting at 1050 °C, slightly below the melting point of the bulk Cu at 1083 °C. Figure 3b illustrates that a few liquid Cu pools had formed at 1182.3 °C. As shown in Figure 3c, the Cu powder has fully melted after holding at 1200 °C for ten minutes, and some isolated oxides in both liquid and solid states were spotted floating on the liquid Cu pool. Figure 3d presents the solidification process of liquid oxides. As the temperature decreased, the crystallization started around the marked oxides and then proceeded in various directions on the surface of the liquid Cu pool. This phenomenon is further evidenced by the detailed inserted images from 1164.8 °C to 1127.0 °C in Figure 3d.
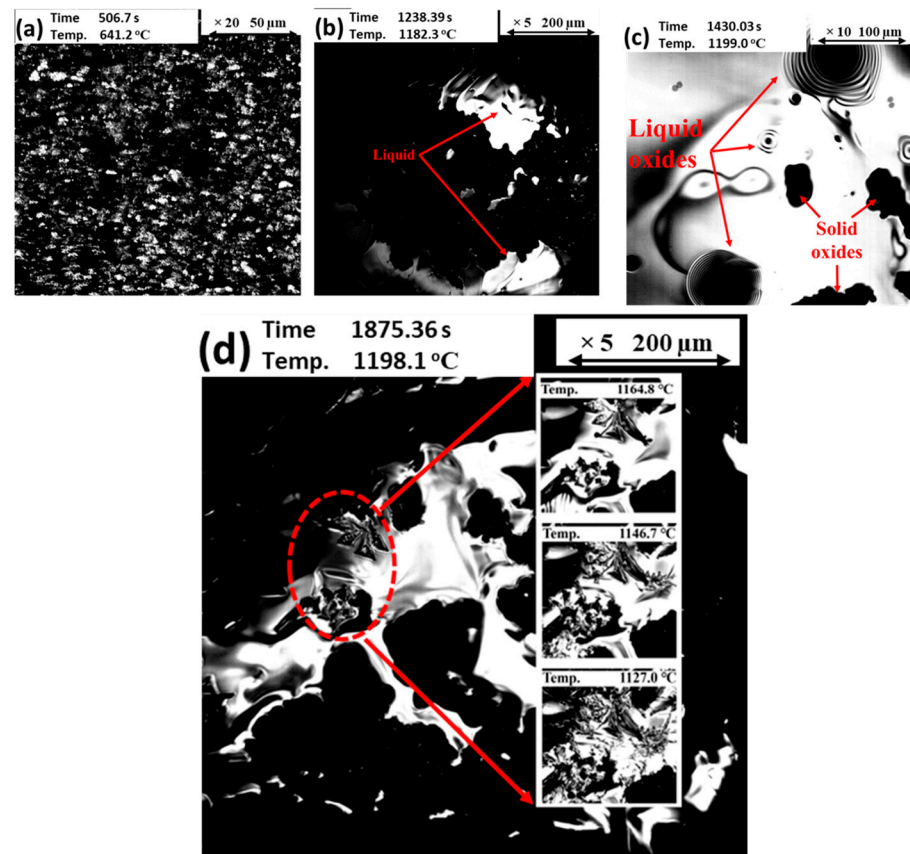

Figure 3. Melting and solidification process of pure Cu-coated sample. (**a**) Cu powder on the surface, (**b**) Melting started, (**c**) Fully melted, (**d**) Solidification.

Figure 4 shows the solidification process of the Cu–Cr coating. The melting point of bulk Cr is around 1907 °C, which is significantly higher than the 1493 °C of bulk Q235. As highlighted within the red dot circle in Figure 4a, a considerable number of solid particles still remained within the liquid phase, even after holding at 1250 °C for ten minutes. These solid particles were later identified as unmelted Cr powders during subsequent material characterization. This phenomenon is substantiated by the extremely low solubility of Cr in Cu. In addition to the unmelted Cr particles, the solid oxide clusters were observed floating

on the liquid surface. The solidification process at 960 °C can be found in Figure 4b. It can be seen that most of the coating remained in the liquid phase, which is assumed to be liquid Cu. It proves that the addition of Cr to the Cu powder has slowed down the solidification of the composite coating. As seen in Figure 4c, most of the liquid had transformed into solids, with some residual liquid nestled between solids at 950 °C.
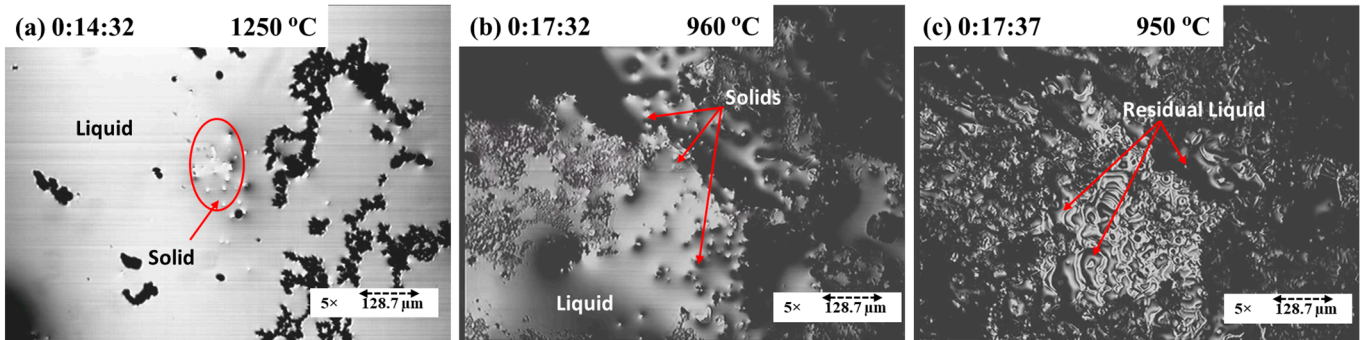

Figure 4. Solidification process of Cu–Cr coating. (**a**) Liquid pool with undissolved solid particles, (**b**) a combination of the solid and liquid phases, (**c**) solidified coating with the lesser residual liquid left.

As per the Cu-Ni phase diagram illustrated in Figure 1, the Cu-Ni solid solution with a 12 %wt Ni should initiate melting at 1137.5 °C. However, the in situ observation in Figure 5a shows that the Cu-Ni powder mixture began to melt at 1099.5 °C, which is far below 1137.5 °C for the Cu-Ni solid solution and marginally higher than 1085 °C for the bulk Cu. This discrepancy provides evidence that the solid-liquid phase transformation of the powder mixture is significantly different from that of the bulk alloy with the same chemical composite, which must be considered in the design of surface alloying. At 1156.7 °C, the melting process became faster. A combination of solid and liquid phases was observed in Figure 5b, which swiftly converted into a liquid pool with minimal solid particles remaining at 1163.6 °C, as illustrated in Figure 5c. Although bulk Ni only started to melt at 1453 °C, the Cu-Ni powder mixture was fully melted at 1175 °C, as shown in Figure 5d. It is vital to report that the melting points observed during this process are higher than that of bulk Cu but significantly lower than that of bulk Ni. The presence of Ni slows down the melting of Cu. Due to Ni's solubility in liquid Cu, the melting point of the Cu-Ni coating is significantly lower than that of bulk Ni. The properties of the substrate also affect the coating's melting and solidification behaviors. Zhao et al. observed that for the same coating material, the coating properties and microstructure varied for aluminum and steel substrates, while the coating parameters were identical [48].
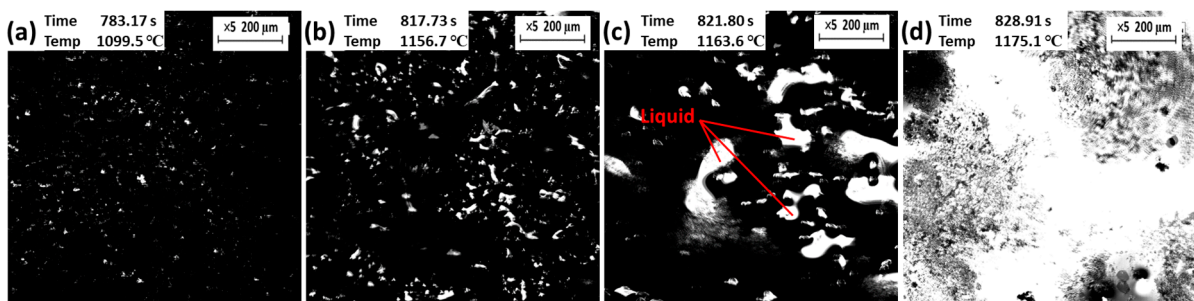

Figure 5. Melting process of Cu-Ni powders. (**a**) Metallic powders started to melt, (**b**) Solid powders with some molten liquid, (**c**) Liquid pool started to form with fewer solid powders left, (**d**) fully melt.

The solidification process of Cu-Ni composite coating on the Q235 substrate is shown in Figure 6. As seen in Figure 6a, after the complete melting of the Cu-Ni powders, some solid and liquid oxides were observed floating on the liquid Cu-Ni solution, with the solid oxides tending to aggregate into clusters. As marked by red dot circles in Figure 6b, the

liquid Cu-Ni solution started solidifying at 1161.8 °C, closely aligned with the liquidus temperature calculated through Thermo-Calc, as indicated in Figure 1. The number of oxide clusters significantly increased and spread on the remaining liquid Cu-Ni solution. When the temperature dropped to 1105.3 °C, as displayed in Figure 6c, the Cu-Ni solid phase significantly grew, and only a few spots of residual liquid Cu-Ni could be observed. The coating was fully solidified when the temperature was reduced to 1090.2 °C, as shown in Figure 6d.
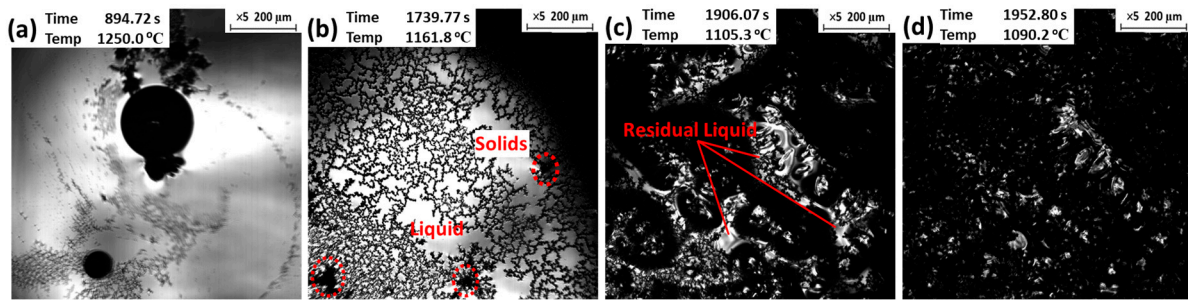

Figure 6. Solidification process of Cu-Ni coating. (**a**) Fully molten state, (**b**) solidification started, (**c**) solidified coating with less molten liquid, (**d**) fully solidified.

3.2. Surface Morphologies of the Coated Samples

Figure 7a,c,e present the overall surface morphologies of three different coated samples, and the red square regions in them were further investigated by secondary electron SEM imaging and displayed in Figure 7b,d,f. It can be found that the pure Cu powder-coated sample shows an undesirable convex surface shape, as seen in Figure 7a. In addition to the gold-shinny Cu appearance, a portion of the coating surface displays a dark color corresponding to the mixture of oxide and solidified Cu observed during HTCLSM. The micro-sized oxide particles can be found in Figure 7b.
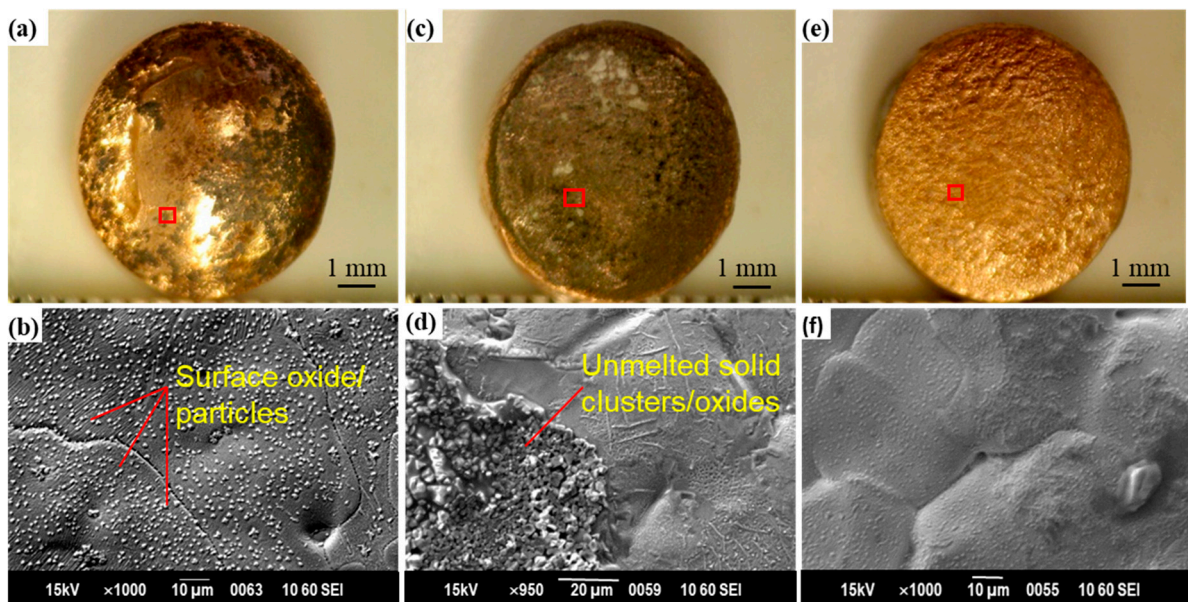

Figure 7. Surface morphologies and secondary electron images of coated samples, (**a**,**b**) pure Cu; (**c**,**d**) Cu–Cr; and (**e**,**f**) Cu-Ni.

As indicated in Figure 7c,d, the Cu–Cr coated sample's surface reveals a porous appearance and unmelted solid clusters/oxides, which is undesirable. In contrast, the surface of the Cu-Ni coated sample shown in Figure 7e,f appears smooth, and no dark region

(oxidation). As shown in Figure 7f, the Cu-Ni coating layer displays fine and uniform polycrystalline structures, providing evidence that an isomorphous Cu-Ni solution was formed from the Cu and Ni powder composite after heating at 1250 °C. The Cu-Ni coated samples exhibit the most satisfactory surface appearance among the three coating combinations.

3.3. Characterization of Coating Structure

3.3.1. Coating Thickness and Defects

Figure 8a displays that the coating thickness deposited on the steel substrate by pure Cu powder is not uniform. The surface tension of the liquid Cu pool tends to drag the liquid Cu to the center of the round specimen, creating a convex layer of 960 μm thick in the center and significantly thinner, around 100 μm, at the edge. A substantial amount of casting porosities, up to 184.75 μm in radius, existed within the coated layer. The formation of porosity defects was attributed to the fact that the sample was heated much higher than the melting temperature of Cu, followed by rapid cooling. The existence of porosity defects significantly worsens the coating quality and can potentially reduce anti-corrosion performance when exposed to an aggressive environment [49]. As observed from the high-magnified view of the interface between the Cu coating layer and the steel substrate in Figure 8d, the Cu penetrated the grain boundary of the steel substrate to a depth of 35 μm.
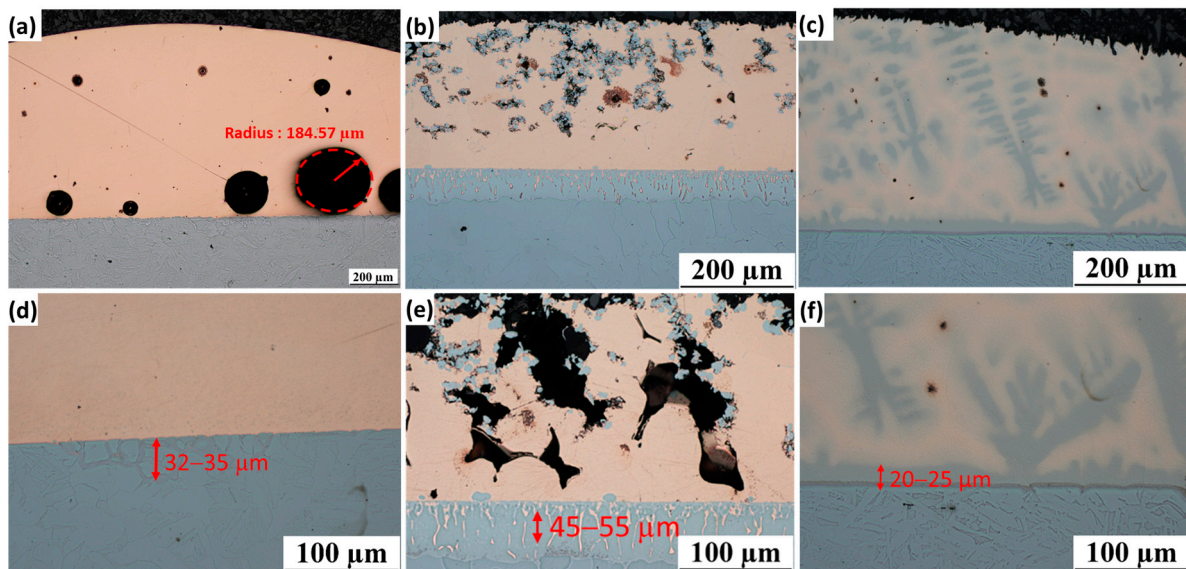

Figure 8. Cross-section of the coating layers at the center of coated samples, (**a**,**d**) pure Cu; (**b**,**e**) Cu–Cr; (**c**,**f**) Cu-Ni.

Despite the formation of a uniformly thick layer for the Cu–Cr coated sample, substantial cavities are visible throughout the coating, as indicated in Figure 8b and further confirmed in Figure 8e. These severe coating defects are caused by the high melting point of Cr and its insolubility in Cu [50]. Furthermore, Cu penetration into the grain boundaries of the steel substrate is up to 55 μm, which is even worse than the pure Cu-coated sample. This phenomenon will be confirmed and explained in the subsequent metallurgical examination.

In contrast, the Cu-Ni composite coatings exhibit a relatively uniform thickness distribution, ranging from 550 μm at the center to 350 μm at the edge, as shown in Figure 8c. It is interesting to report that a dendritic casting structure can be found in the Cu-Ni coating layer. It can be found in Figure 8f that a transition layer of 20–25 μm had formed between the Cu-Ni coating and the steel substrate. This transition layer is expected to be a Ni-rich region due to the high affinity of Ni towards Fe as compared to Cu's lack of miscibility with Fe. Ni plays an essential role in securing the bonding integrity of the coating and minimization of Cu penetration into the parent steel. A detailed metallurgical examination can be found in the following session.

3.3.2. Coating Structure and Integrity at Coating and Substrate Interface

While Cu is a primary element used to combat corrosion in the proposed metallic surface alloying technique due to its low cost, hot shortness can occur during the hot forming of Cu-containing steel. Therefore, introducing the Cr and Ni alloy elements and forming a diffused interface between the anti-corrosion metallic compound (instead of pure Cu) and the steel substrate is vital. This not only provides bonding strength but also suppresses Cu penetration into the parent steel.

Figure 9 shows distinct evidence of penetration and flow of liquid Cu into austenite grain boundaries of the Q235 substrate under pure Cu surface alloying. It is important to note that the mechanism of Cu enrichment for the surface alloying technique is different from that of Cu-containing steel. During the surface alloying, the Cu did not diffuse from the bulk steel and precipitated into the austenite grain boundaries of the steel. Instead, liquid Cu attracted the steel substrate and penetrated the austenite grain boundaries of the steel substrate. Figure 9b presents the EDS layered map and its corresponding Cu/Fe elemental maps. It can be found that the penetrated liquid Cu tended to detach steel grains from the metal surface. This phenomenon is known as liquid metal corrosion or liquid metal embrittlement [51,52]. Based on the reference [53], the penetration of liquid Cu into grain boundaries of substrate steel occurs rapidly. In general, although the Cu coating was successfully deposited on the steel surface, the significant Cu enrichment and penetration along grain boundaries of the steel substrate could trigger the hot shortness and surface cracking during the subsequent hot forming process. Hence, the surface alloying of pure Cu powder is undesirable due to the occurrence of liquid metal corrosion.
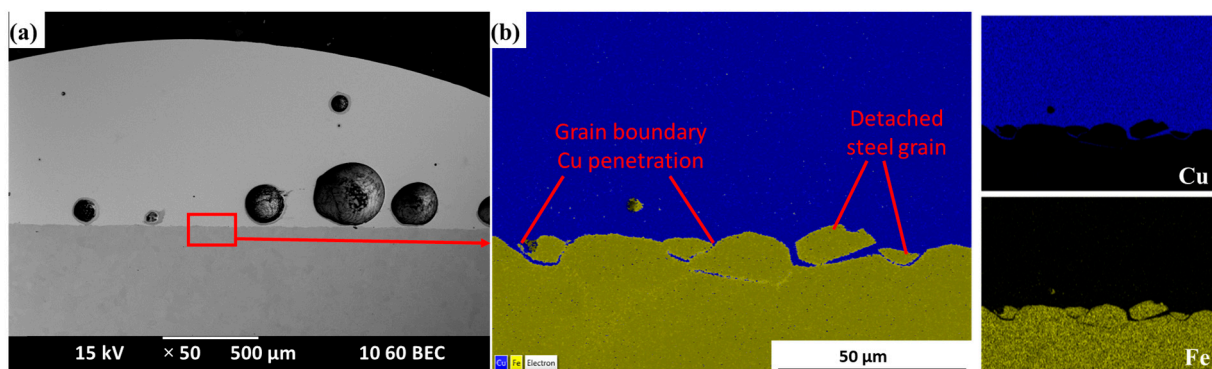

Figure 9. Pure Cu coating structure (**a**) Secondary Electron Image, (**b**) EDS layered map, and its Cu and Fe elemental maps.

As shown in Figure 10, the cross-section of the Cu–Cr coated sample consists of three distinct regions: the coating layer, diffusion zone, and substrate. It can be found that Cu and Cr elements did not form a homogeneous solution at the designed composition and thermal excursion history. The Cr particles remained unmelted and can still be observed within the Cu-based coating layer. The Fe element diffused from the steel matrix was combined with unmelted Cr particles to form a Cu-depleted Fe–Cr phase, as indicated in Figure 10a,b. These Fe–Cr phases tended to gather together, which was observed as the cluster in Cu–Cr coating. The presence of the Fe–Cr clusters introduced an inhomogeneous structure to the coating layer, potentially compromising the anti-corrosion performance.

More importantly, it is crucial to note that despite Cr diffusing into the steel matrix to form a Cr-rich transition zone around 45~55 μm between the coating layer and the substrate, it also facilitated Cu penetration into the grain boundaries, as indicated in Figure 10c,d. This phenomenon is attributed to the chemical actions among Fe, Cr, and Cu at the transition region. The Fe–Cu system is immiscible, and the same holds for the insolubility of Cu and Cr elements [50]. Consequently, the L(Cu), α(Fe,Cr), and γCu phases were expected to coexist during the surface alloy at the temperature range of 1100–1250 °C [54]. The insolubility of liquid Cu and α(Fe,Cr) resulted in the penetration of liquid Cu into the

grain boundaries of the substrate. This observation confirms that Cu–Cr surface alloying is unable to prevent liquid Cu penetration, which could cause hot shortness in the subsequent forming process.
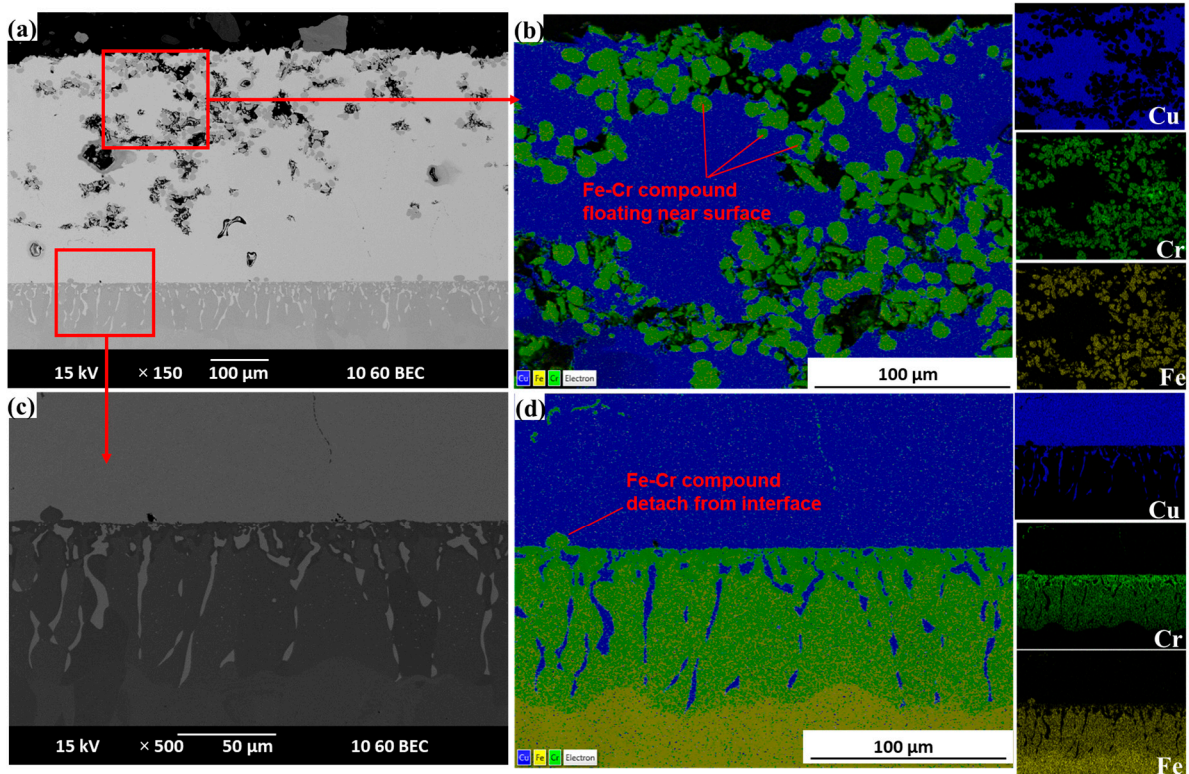

Figure 10. Cu–Cr coating structure (**a**) Back-scattered Electron Microscopic Image, (**b**) EDS layered map of the surface region. (**c**) Back-scattered electron image and (**d**) EDS layered map of the interface region. Cu, Cr, and Fe elemental maps for (**b**,**d**) are shown on the right side of respective EDS layered maps.

The microstructure of the metallic coating formed by the proposed Cu-Ni surface alloying techniques can be found in Figure 11. The sample exhibits three regions, including the cupronickel coating, a continuous binding transition layer between the cupronickel coating and the substrate, and the Q235 steel substrate. The Cu and Ni homogenously coexisted at the Cu-Ni coating, which confirmed the nature of the cupronickel solution alloy. As evidenced by elemental spectrums of the point scan in Figure 11a,e, the chemical composition of deposited cupronickel coating was 89.3 wt% Cu, 6.2 wt% Ni, and 4.5 wt% Fe. Compared with the initial metallic powder composite of 87.5 wt% Cu and 12.5 wt% Ni, the weight percentage of Ni is slightly reduced. As shown in Figure 11a, the dendritic phases were formed within the cupronickel coating. The elemental maps in Figure 11b display that the dendrites are rich in Ni and Fe and depleted in Cu, confirming the FeNi phase. At the elevated temperature of 1250 °C, the Fe could be dissolved into the cupronickel solution via two possible mechanisms, i.e., (1) Fe elements from the steel substrate could diffuse into the melted coating composite; and/or (2) the steel grains could be detached from the base metal by liquid metal corrosion [51]. Regardless of the source, the Fe element reacted with the Ni element during the solidification process due to the high affinity of Fe towards Ni as compared to Cu, resulting in the formation of a new phase that solidifies into a dendritic structure. The chemical composition of dendrites consisted of 62.7% Cu, 19.3 wt% Ni, and 18.1 wt% Fe, as seen in Figure 11f. It is important to note that Cu concentrations remained high in both of the cupronickel solutions or dendrites. At the same time, the Ni percentage is comparatively higher in dendrites when compared to the rest of the coating.
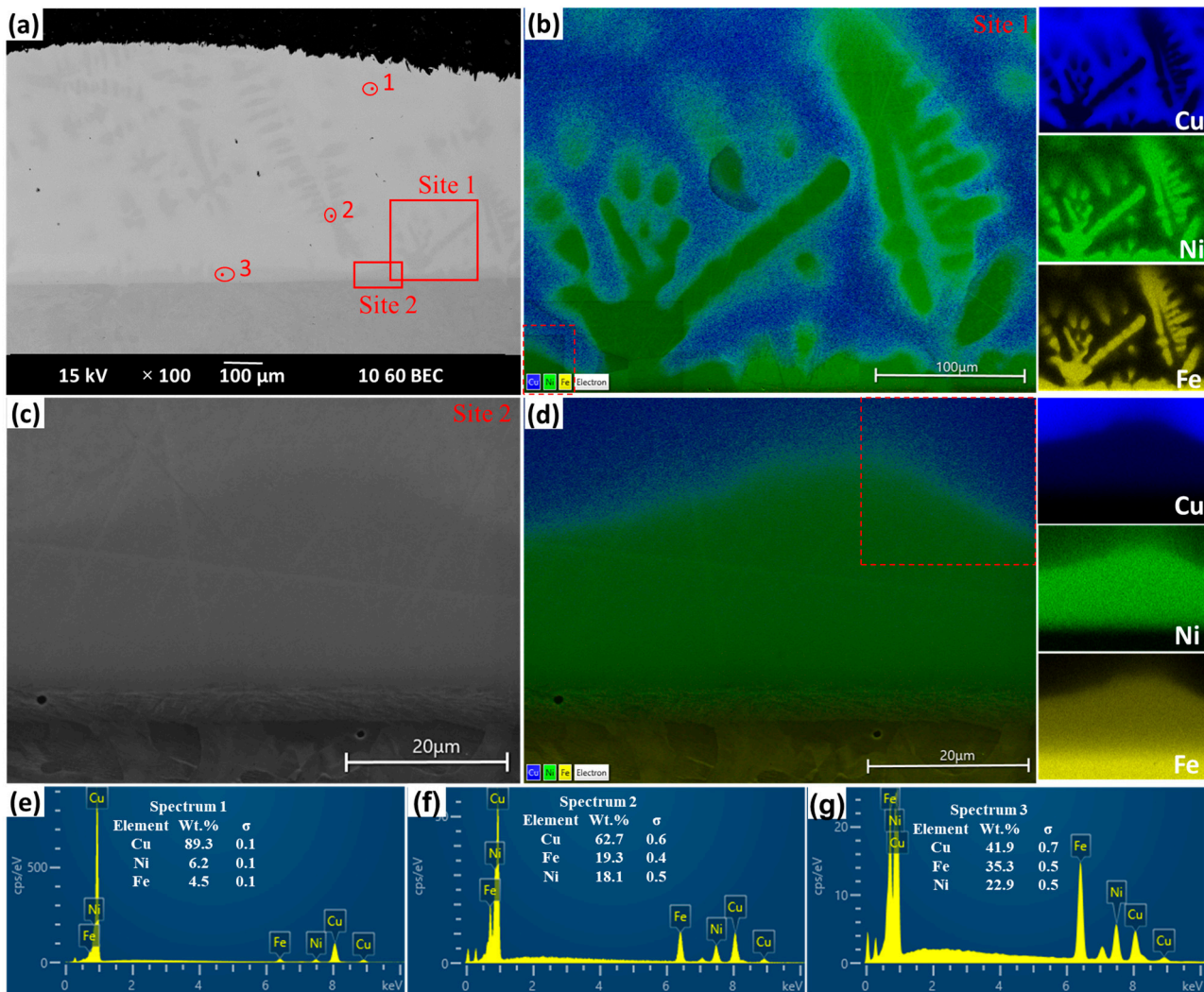
Figure 11. Cu-Ni coating structure (**a**) Back-scattered Electron Image, (**b**) EDS layered map and Elemental maps of Cu, Ni, and Fe at Site 1 (Ni-rich dendritic structure), (**c**) Back-scattered Electron Image of Site 2 (Ni-rich interface); (**d**) EDS layered map and Elemental maps of Cu, Ni, and Fe at Site 2 (Ni-rich interface); (**e**–**g**) Elemental spectrums of Point scan 1 (coating region), (**f**) point scan 2 (dendrite), (**g**) point scan 3 (interface). In (**a**), an overlapping region between Site 1 and Site 2 is highlighted by the red dashed rectangular boxes in the EDS mapping shown in (**b**,**d**).

Although the thickness of the cupronickel coating is up to 500 μm, as shown in Figure 11a, the thickness of the binding transition layer between the cupronickel coating and the substrate is around 20–25 μm. The EDS mapping results depicted in Figure 11d confirm that the binding transition layer is enriched with Ni. The chemical composition of the Ni-rich transition layer was analyzed through elemental spectrum scanning in Figure 11g, revealing a composition of 41.9 wt% Cu, 22.9 wt% Ni, and 35.3 wt% Fe. The formation of the Ni-rich transition layer and the high percentage of Cu in the Ni-rich transition layer align with the expected behavior of a ternary Cu-Ni–Fe system. Both liquid L Cu-Ni–Fe and solid γ Cu-Ni–Fe phases coexist when a Cu-Ni–Fe system is exposed to high temperatures. The L phase with a lower Ni/Cu ratio flows upwards to form the cupronickel coat. The γ Cu-Ni–Fe solution phases with a higher Ni/Cu ratio are more enriched on an interface to promote the Ni-rich transition layer. It is interesting to report that even though the Cu concentrations are different in the coating and transition layer, there are still relatively high Cu concentrations of 41.9 wt% in the Ni-rich transition layer [13]. The Ni-rich interface layer is continuous and adhesive, effectively preventing

Cu penetration into the substrate grain boundaries, which is a desirable characteristic in surface alloying.

It is intriguing to compare the characteristics of the transition layers formed by the Cu–Cr and Cu-Ni composites. Rothman et al. [55] measured the simultaneous lattice diffusion of Fe, Cr, and Ni, revealing that the diffusion coefficient of Cr is 1.39 times that of Fe and 2.5 times of Ni. Consequently, the Cr can diffuse deeper into the steel matrix compared to Ni. It aligns well with current research that the Cr-rich transition zone formed by the Cu–Cr coating has a thickness ranging from 45–55 μm, almost double the thickness of the Ni-rich transition layer observed in the Cu-Ni coating (20–25 μm). However, despite its thickness, the Cr-rich transition layer is unable to prevent Cu penetration during surface alloying at high temperatures. In contrast, the Ni-rich transition layer is capable of minimizing the risk of Cu penetration.

The material characterization confirms that the surface alloying technique utilizing Cu-Ni powder at high temperature successfully forms a coating comprising cupronickel solution and FeNi dendrites. In addition, a Ni-rich transition layer acts as a chemical binding between the cupronickel coating and the steel substrate, which plays a critical role in reducing liquid Cu penetration at the steel grain boundary to minimize the risk of hot shortness during subsequent metal forming.

The significant difference in coating performance results from the types of bond interaction between Cr and Ni in the structures of Cu–Cr and Cu-Ni alloys. Copper and chromium have different atomic radii and crystalline structures (Cu has an fcc structure, while Cr has a bcc structure). In contrast, nickel is similar to copper in terms of atomic size and crystal structure, with both having fcc structures. The electronegativity difference between Cu and Cr is greater than that between Cu and Ni, leading to stronger metallic bonds in Cu-Ni alloys and some covalent character in Cu–Cr alloys. The similar atomic sizes and electronegativity and the identical fcc structures of Cu and Ni facilitate the formation of solid solutions. In contrast, the differing atomic sizes, electronegativity, and crystalline structures of Cu and Cr result in limited solubility and the formation of distinct phases.

In future studies, it will be beneficial to investigate the optimized structures of Fe–Cr and compare the stabilized energies of Fe–Cr, Cu–Cr, and Cu-Ni at the temperatures of interest.

3.4. Coating Formation in Practical Hot Rolling and Corrosion Resistance Performance

To evaluate the proposed surface alloy technique, a series of hot rolling experiments were conducted using a TMAX tube furnace manufactured by Xiamen Tmax Battery Equipments Limited, Xiamen, China, and an experimental Hille 100 rolling mill manufactured by Hille Engineering Company Ltd., Sheffield, UK.

The data collected from the high-temperature confocal laser scanning microscopy indicated a suitable temperature range of 1099.5–1175 °C for melting the mixture of 87.5 wt% Cu and 12.5 wt% Ni powders. Hence, a heating temperature of 1150 °C was selected to mimic the actual reheating condition of an industry hot strip rolling mill. The process involved covering 20 mm thick Q235 steel slabs with Cu-Ni metallic powders, which were then heated in a tube furnace filled with argon gas to 1150 °C and held at that temperature for 25 min to facilitate the surface alloying technique. Subsequently, a 20% reduction was applied to the heated slabs immediately after removing them from the furnace. The rolled samples were air-cooled to room temperature.

Figure 12a displays a representative cross-section image of the coated slab after hot rolling, revealing the formation of a compact metallic coating with an average thickness of 220 μm. The line-scan analysis in Figure 12b shows a sharp increase in copper intensity from the transition region, which remains high throughout the coating layer. The intensities of Ni and Fe were nearly identical across the coating layer, aligning with HTCLSM's results in Figure 11e, consisting of nearly the same amount of 6.2 wt% Ni and 4.5 wt% Fe in the coating layer. Fe intensity increases gradually towards the steel matrix, while Ni tends to concentrate at the interface.
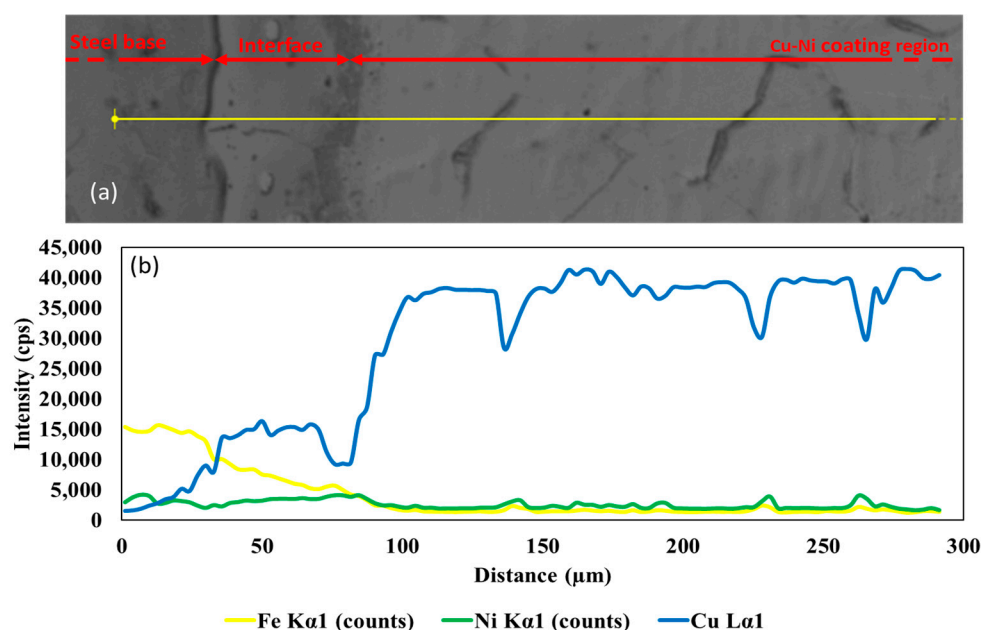
Figure 12. (**a**) Cu-Ni coated sample cross-section after practical hot rolling and (**b**) line-scan of the cross-section.

To investigate the effectiveness of cupronickel-coated steel in terms of anti-corrosion performance, a series of electrochemical corrosion tests were conducted in a 3.5% NaCl solution using a Gamry electrochemical corrosion testing rig over a period of 10 min, 1 day, 7 days, 14 days, and 30 days. The tests were performed on both cupronickel-coated steel and uncoated bare steel for comparison. Figure 13 presents the typical polarization curves after 1 week of salted water immersion. The results confirmed the superior corrosion-resistive properties of the Cu-Ni coating compared to uncoated Q235 steel. The corrosion rate of the coated sample was calculated to be 33.42 μm/yr., which is 44% lower than that of the uncoated sample, recorded to be 59.78 μm/yr. These findings indicate a significant improvement in corrosion resistance with the application of the Cu-Ni coating.

In summary, in situ thermal interactions of three composites, including pure Cu powder, a mixed powder of 87.5 wt% Cu-12.5 wt% Ni, and a mixed powder of 90 wt% Cu-10 wt% Cr, were tested using a HTCLSM, considering the maximum hot working temperatures of steel in the industry (1200–1250 °C). The Cu-Ni powder mixture began to melt at 1099.5 °C and was fully melted at 1175 °C, significantly different from the Cu-Ni solid solution and bulk Cu or Ni. As a result of high-temperature reactions, copper penetration of up to 35 μm for pure copper and 55 μm for copper-chromium composite coatings occurred due to liquid metal corrosion. In contrast, the Cu-Ni metallic powder combination ensures a cupronickel solution coating, with a chemical composition of 89.3 wt% Cu, 6.2 wt% Ni, and 4.5 wt% Fe, which inhibits copper penetration. The cupronickel coating presents uniform thickness, superior surface morphology, and continuous coverage. A 44% improvement in corrosion resistance was confirmed by electrochemical corrosion tests.

To achieve an effective corrosion-resistant layer, current research suggests optimizing the specific components of Cu and Ni, with a composite ratio of 7:1 (Cu:Ni). However, future studies should explore the synergistic effects of multi-element alloying, including Cr, Ni, Cu, and others, to further enhance corrosion resistance. The detailed electrochemical corrosion tests on various Cu, Cu–Cr, and Cu-Ni composite coatings, along with the impact of uneven coatings and the presence of defects on corrosion resistance, will be addressed in a forthcoming report.
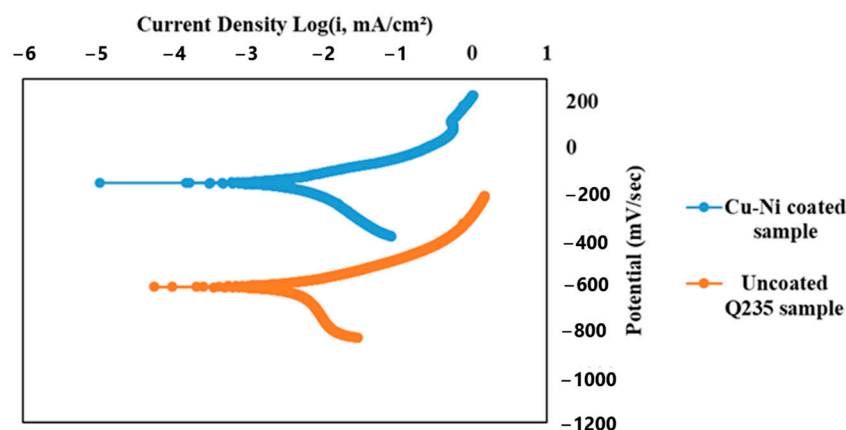
Figure 13. Electrochemical corrosion test results in 3.5% salt solution.

4. Conclusions

A high-temperature surface alloying technology was developed to implement the Cu-based metallic coating on carbon steel surfaces to improve corrosion resistance.

The metallic coatings could be formed on the steel surface due to a high-temperature reaction. However, the pure Cu and Cu–Cr metallic powder combinations were unsuitable due to excessive Cu penetration. The Cu-Ni metallic powder combination demonstrated a high coating quality providing full surface coverage, a consistent coating thickness, and no Cu penetration into grain boundaries.

The surface alloying using a Cu-Ni composite comprised a cupronickel solution coat with FeNi dendrites and a Ni-rich transition layer. The presence of the Ni-rich transition layer is of significant importance as it inhibited Cu from penetrating the steel matrix grain boundary while simultaneously enhancing the adhesion between the coating and the substrate.

The integrity of the coating was further confirmed by hot rolling experiments. The electrochemical corrosion test proved that the Cu-Ni coating exhibited a significantly higher corrosion resistance, with a 44% improvement compared to uncoated Q235 steel.

Author Contributions: Conceptualization, H.Z. and W.W.; methodology, H.H.K., T.W., H.L., L.S.; software, T.W.; validation, H.H.K. and Q.Z.; formal analysis, H.H.K. and H.Z.; investigation, H.H.K., L.S. and H.Z.; resources, A.Y., Z.L.; writing—original draft preparation, H.H.K. and H.Z.; writing—review and editing, H.H.K. and H.Z.; supervision, H.L. and H.Z.; project administration, A.Y., Z.L., W.W. and H.Z.; funding acquisition, A.Y., Z.L., W.W. and H.Z. All authors have read and agreed to the published version of the manuscript.

Institutional Review Board Statement: Not applicable.

Informed Consent Statement: Not applicable.

Data Availability Statement: Data will be made available on request.

Conflicts of Interest: The authors Huda Hanif Khan, Tong Wang, Lihong Su, Huijun Li, Qiang Zhu, Hongtao Zhu declare no conflict of interest. The authors Ana Yang, Zigang Li, Wei Wang are currently employed by Baowu Steel Group Corporation and were employed by Baowu Steel Group Corporation while contributing to this manuscript. Their contributions to this work and manuscript were approved by Baowu Steel Group Corporation, and this manuscript was reviewed and approved by Baowu Steel Group Corporation. They received no financial compensation from any source for the contributions they made to the scientific work and manuscript.

References

1. Wang, Y.; Liu, W.; Li, N.; Zheng, C. The Importance of Structure and Corrosion Resistance of Steels/Alloys. *Coatings* **2022**, *12*, 997. [CrossRef]
2. Exarchos, D.A.; Sima, A.; Ananiadis, E.A.; Dalla, P.T.; Tragazikis, I.K.; Kordatou, T.Z.; Farmaki, S.; Gontzamanis, A.; Kechagias, V.; Kechagias, L.; et al. Development and characterization of environmentally friendly multifunctional protective coatings. *Proc. SPIE* **2022**, *12049*, 102–116.
3. Shevchenko, V.Y.; Shilova, O.A.; Kochina, T.A.; Barinova, L.D.; Belyi, O.V. Improving the Safety of the Transportation System and Resource Conservation through the Introduction of Environmentally Safe Protective Coatings. *Glass Phys. Chem.* **2019**, *45*, 1–9. [CrossRef]
4. Bangaru, N.V.; Krutenat, R.C. Diffusion coatings of steels: Formation mechanism and microstructure of aluminized heat-resistant stainless steels. *J. Vac. Sci. Technol. B Microelectron. Process. Phenom.* **1984**, *2*, 806–815. [CrossRef]
5. Wang, Z.B.; Lu, J.; Lu, K. Chromizing behaviors of a low carbon steel processed by means of surface mechanical attrition treatment. *Acta Mater.* **2005**, *53*, 2081–2089. [CrossRef]
6. Wang, D.; Shi, Z. Aluminizing and oxidation treatment of 1Cr18Ni9 stainless steel. *Appl. Surf. Sci.* **2004**, *227*, 255–260. [CrossRef]
7. Kula, P.; Pietrasik, R.; Dybowski, K. Vacuum carburizing—Process optimization. *J. Mater. Process. Technol.* **2005**, *164–165*, 876–881. [CrossRef]
8. Sun, M.; Du, C.; Liu, Z.; Liu, C.; Li, X.; Wu, Y. Fundamental understanding on the effect of Cr on corrosion resistance of weathering steel in simulated tropical marine atmosphere. *Corros. Sci.* **2021**, *186*, 109427. [CrossRef]
9. Zhang, J.; Zhang, W.; Wei, L.; Pu, L.; Liu, J.; Liu, H.; Li, Y.; Fan, J.; Ding, T.; Guo, Z. Alternating Multilayer Structural Epoxy Composite Coating for Corrosion Protection of Steel. *Macromol. Mater. Eng.* **2019**, *304*, 1900374. [CrossRef]
10. Anagri, A.; Baitukha, A.; Debiemme-Chouvy, C.; Lucas, I.T.; Pulpytel, J.; Tran, T.T.M.; Tabibian, S.; Arefi-Khonsari, F. Nanocomposite coatings based on graphene and siloxane polymers deposited by atmospheric pressure plasma. Application to corrosion protection of steel. *Surf. Coat. Technol.* **2019**, *377*, 124928. [CrossRef]
11. Choi, Y.-S.; Shim, J.-J.; Kim, J.-G. Effects of Cr, Cu, Ni and Ca on the corrosion behavior of low carbon steel in synthetic tap water. *J. Alloys Compd.* **2005**, *391*, 162–169. [CrossRef]
12. Salter, W.J.M. Discussion on surface hot shortness of mild steel. *J. Iron Steel Inst.* **1962**, *200*, 750–751.
13. Akamatsu, S.; Senuma, T.; Takada, Y.; Hasebe, M. Effect of nickel and tin additions on formation of liquid phase in copper bearing steels during high temperature oxidation. *Mater. Sci. Technol.* **1999**, *15*, 1301–1307. [CrossRef]
14. Yamamoto, K.I.; Toh, T.; Hamatani, H.; Tsunenari, K.; Umetsu, K.; Maruki, Y.; Takeuchi, S.; Yamada, Y. Development of steel surface melting technology for improvement of hot shortness caused by tramp elements. *Nippon Steel Tech. Rep.* **2013**, *104*, 69–73.
15. Uhlig, H.H. Passivity in Copper-Nickel and Molybdenum-Nickel-Iron Alloys. *Trans. Electrochem. Soc.* **1944**, *85*, 307. [CrossRef]
16. Ezuber, H.; Al-Shater, A.; Murra, F.; Al-Shamri, N. Corrosion Behavior of Copper-Nickel Alloys in Seawater Environment. In Proceedings of the 16th Middle East Corrosion Conference & Exhibition, Manama, Bahrein, 8–11 February 2016.
17. Tolulope Loto, R. Correlative investigation of the corrosion susceptibility of C70600 and C26000 copper based alloys for application in seawater environment. *Mater. Today Proc.* **2022**, *65*, 2151–2155. [CrossRef]
18. Qian, Y.H.; Niu, D.; Xu, J.J.; Li, M.S. The influence of chromium content on the electrochemical behavior of weathering steels. *Corros. Sci.* **2013**, *71*, 72–77. [CrossRef]
19. Park, S.A.; DLe, P.; Kim, J.G. Alloying Effect of Chromium on the Corrosion Behavior of Low-Alloy Steels. *Mater. Trans.* **2013**, *54*, 1770–1778. [CrossRef]
20. Hosmani, S.S.; Kuppusami, P.; Goyal, R.K. (Eds.) Basics of Surface Alloying. In *An Introduction to Surface Alloying of Metals*; Springer: New Delhi, India, 2014; pp. 1–28.
21. Ezaki, H.; Nambu, T.; Ninomiya, R.; Nakahara, Y. Estimation of liquidus temperature of Sn-based alloys and its application to the design of Pb-free solder. *J. Mater. Sci. Mater. Electron.* **2002**, *13*, 269–272. [CrossRef]
22. Djurdjevic, M.; Manasijević, S.; Odanović, Z.; Dolić, N. Calculation of Liquidus Temperature for Aluminum and Magnesium Alloys Applying Method of Equivalency. *Adv. Mater. Sci. Eng.* **2013**, *2013*, 170527. [CrossRef]
23. Jia, Y.; Cheng, H.; Qiu, J.; Han, F. Effect of temperature on diffusion behavior of Te into nickel. *J. Nucl. Mater.* **2013**, *441*, 372–379. [CrossRef]
24. Ling, Z.; Wang, M.; Kong, L. Liquid Metal Embrittlement of Galvanized Steels During Industrial Processing: A Review. In *Transactions on Intelligent Welding Manufacturing*; Springer: Singapore, 2018; pp. 25–42.
25. Jeon, W.-S.; Sharma, A.; Jung, J.P. Liquid Metal Embrittlement of Galvanized TRIP Steels in Resistance Spot Welding. *Metals* **2020**, *10*, 787. [CrossRef]
26. Ikeda, Y.; Yuan, R.; Chakraborty, A.; Ghassemi-Armaki, H. Early stages of liquid-metal embrittlement in an advanced high-strength steel. *Mater. Today Adv.* **2022**, *13*, 100196. [CrossRef]
27. Liu, T.; Long, M.; Chen, D.; Wu, S.; Tang, P.; Liu, S.; Duan, H.; Yang, J. Investigations of the peritectic reaction and transformation in a hypo-peritectic steel: Using high-temperature confocal scanning laser microscopy and differential scanning calorimetry. *Mater. Charact.* **2019**, *156*, 109870. [CrossRef]
28. Ikhmayies, S. Using thermo-calc software to produce the phase diagram of Zn-Te system. *J. Energy Syst.* **2020**, *4*, 88–95. [CrossRef]
29. Shah, S.; Ullah, N.; Ullah, B.; Khan, M.S. Thermodynamic Analysis and Calculations of (Fe-Co) Alloy by Modeling and Simulation using Thermo-Calc Software. *J. Heterocycl.* **2018**, *1*, 35–38. [CrossRef]

30. Chikama, H.; Shibata, H.; Emi, T.; Susuki, M. "In-situ" real time observation of planar to cellular and cellular to dendritic transition of crystals growing in Fe–C alloy melts. *Mater. Trans. JIM* **1996**, *37*, 620–626. [CrossRef]

31. Ren, Y.; Zhu, P.; Ren, C.; Liu, M. Dissolution of SiO2 Inclusions in CaO-SiO2-Based Slags In Situ Observed Using High-Temperature Confocal Scanning Laser Microscopy. *Metall. Mater. Trans. B* **2022**, *53*, 682–692. [CrossRef]

32. Michelic, S.; Goriupp, J.; Feichtinger, S.; Kang, Y.B.; Bernhard, C.; Schenk, J. Study on Oxide Inclusion Dissolution in Secondary Steelmaking Slags using High Temperature Confocal Scanning Laser Microscopy. *Steel Res. Int.* **2016**, *87*, 57–67. [CrossRef]

33. Böhme, N.; Hauke, K.; Dohrn, M.; Neuroth, M.; Geisler, T. High-temperature phase transformations of hydroxylapatite and the formation of silicocarnotite in the hydroxylapatite–quartz–lime system studied in situ and in operando by Raman spectroscopy. *J. Mater. Sci.* **2022**, *57*, 15239–15266. [CrossRef]

34. Branch, S.D.; Felmy, H.M.; Medina, A.S.; Bryan, S.A.; Lines, A.M. Exploring the Complex Chemistry of Uranium within Molten Chloride Salts. *Ind. Eng. Chem. Res.* **2023**, *62*, 14901–14909. [CrossRef]

35. Zhang, B.; Tekle, H.; O'Malley, R.J.; Sander, T.; Smith, J.D.; Gerald II, R.E.; Huang, J. In Situ and Real-Time Mold Flux Analysis Using a High-Temperature Fiber-Optic Raman Sensor for Steel Manufacturing Applications. *J. Light. Technol.* **2023**, *41*, 4419–4429. [CrossRef]

36. Zhang, B.; Tekle, H.; O'Malley, R.J.; Smith, J.D.; Gerald II, R.E.; Huang, J. In Situ High-Temperature Raman Spectroscopy via a Remote Fiber-Optic Raman Probe. *IEEE Trans. Instrum. Meas.* **2023**, *72*, 6002008. [CrossRef]

37. Galedari, S.A.; McDonald, A. A Comprehensive Review of Corrosion Resistance of Thermally-Sprayed and Thermally-Diffused Protective Coatings on Steel Structures. *J. Therm. Spray Technol.* **2019**, *28*, 645–677. [CrossRef]

38. Oskay, C.; Meisner, T.M.; Dobler, C.; Grégoire, B.; Galetz, M.C. Scale Formation and Degradation of Diffusion Coatings Deposited on 9% Cr Steel in Molten Solar Salt. *Coatings* **2019**, *9*, 687. [CrossRef]

39. Boulesteix, C.; Pedraza, F. Characterisation of aluminium diffusion coatings elaborated on austenitic stainless steels and on ferritic-martensitic steels. *Surf. Coat. Technol.* **2018**, *339*, 27–36. [CrossRef]

40. Grinon-Echaniz, R.; Refait, P.; Jeannin, M.; Sabot, R.; Paul, S.; Thornton, R. Study of cathodic reactions in defects of thermal spray aluminium coatings on steel in artificial seawater. *Corros. Sci.* **2021**, *187*, 109514. [CrossRef]

41. Wu, J.; Zhang, S.D.; Sun, W.H.; Wang, J.Q. Influence of oxidation related structural defects on localized corrosion in HVAF-sprayed Fe-based metallic coatings. *Surf. Coat. Technol.* **2018**, *335*, 205–218. [CrossRef]

42. Takeuchi, S.; Ito, M.; Takeda, K. Modelling of residual stress in plasma-sprayed coatings: Effect of substrate temperature. *Surf. Coat. Technol.* **1990**, *43–44*, 426–435. [CrossRef]

43. *ASTM A588/A588M-19*; Standard Specification for High-Strength Low-Alloy Structural Steel, up to 50 ksi [345 MPa] Minimum Yield Point, with Atmospheric Corrosion Resistance. ASTM: West Conshohocken, PA, USA, 2019; p. 3.

44. Vattur Sundaram, M.; Karamchedu, S.; Gouhier, C.; Hryha, E. Vacuum sintering of chromium alloyed powder metallurgy steels. *Met. Powder Rep.* **2019**, *74*, 244–250. [CrossRef]

45. Morcillo, M.; Chico, B.; Cano, H.; de la Fuente, D. Weathering steels: From empirical development to scientific design. A review. *Corros. Sci.* **2014**, *83*, 6–31. [CrossRef]

46. Wang, W. Review on studies of reducing Cu-induced surface hot shortness in steel. *Baosteel Tech. Res.* **2015**, *9*, 3–13.

47. Servant, C.; Sundman, B.; Lyon, O. Thermodynamic assessment of the Cu Fe Ni system. *Calphad* **2001**, *25*, 79–95. [CrossRef]

48. Zhao, Y.; Yu, Z.; Planche, M.P.; Lasalle, A. Influence of Substrate Properties on the Formation of Suspension Plasma Sprayed Coatings. *J. Therm. Spray Technol.* **2018**, *27*, 73–83. [CrossRef]

49. Zhang, S.D.; Wu, J.; Qi, W.B.; Wang, J.Q. Effect of porosity defects on the long-term corrosion behaviour of Fe-based amorphous alloy coated mild steel. *Corros. Sci.* **2016**, *110*, 57–70. [CrossRef]

50. Ma, E. Alloys created between immiscible elements. *Prog. Mater. Sci.* **2005**, *50*, 413–509. [CrossRef]

51. Zhang, J.; Hosemann, P.; Maloy, S. Models of liquid metal corrosion. *J. Nucl. Mater.* **2010**, *404*, 82–96. [CrossRef]

52. Balbaud-Célérier, F.; Courouau, J.L.; Feron, D.; Martinell, L. Corrosion of structural materials by liquid metals used in fusion, fission, and spallation. In *Nuclear Corrosion*; Ritter, S., Ed.; Woodhead Publishing: Sawston, UK, 2020; pp. 437–457.

53. Shibata, K.; Seo, S.J.; Kaga, M.; Uchino, H.; Sasanuma, A.; Asakura, K.; Nagasaki, C. Suppression of surface hot shortness due to Cu in recycled steels. *Mater. Trans.* **2002**, *43*, 292–300. [CrossRef]

54. Dreval', L.; Turchanin, M.A.; Abdulov, A.R.; Bondar, A.A. Thermodynamic assessment of the Cu–Fe–Cr phase diagram. *Chem. Met. Alloys* **2010**, *3*, 132–139. [CrossRef]

55. Rothman, S.; Nowicki, L.; Murch, G. Self-diffusion in austenitic Fe-Cr-Ni alloys. *J. Phys. F Met. Phys.* **1980**, *10*, 383. [CrossRef]